

Pulsed Infrared Emission from Magnetar 4U 0142+61 Detected by JWST

JEREMY HARE,^{1,2,3} GEORGE G. PAVLOV,⁴ BETTINA POSSELT,^{5,4} GEORGE YOUNES,^{1,6} AND OLEG KARGALTSEV⁷

¹*NASA Goddard Space Flight Center, Greenbelt, MD 20771, USA*

²*Center for Research and Exploration in Space Science and Technology, NASA/GSFC, Greenbelt, Maryland 20771, USA*

³*The Catholic University of America, 620 Michigan Ave., N.E. Washington, DC 20064, USA*

⁴*Department of Astronomy & Astrophysics, Pennsylvania State University, 525 Davey Lab, University Park, PA 16802, USA*

⁵*Department of Astrophysics, University of Oxford, Denys Wilkinson Building, Keble Road, Oxford OX1 3RH, UK*

⁶*Center for Space Sciences and Technology, University of Maryland, Baltimore County, Baltimore, MD 21250, USA*

⁷*Department of Physics, The George Washington University, 725 21st St. NW, Washington, DC 20052*

ABSTRACT

We report on a JWST observation of the magnetar 4U 0142+61 on 2024 August 18 with the Near-Infrared Camera (NIRCam). NIRCam observed the magnetar for 33 min in timing mode, providing a time resolution of 2.5 s. In the F410M filter (pivot wavelength 4.08 μm), we measured the flux density $f_\nu = 22.9 \pm 0.6 \mu\text{Jy}$ and detected pulsations at a frequency of $115.059 \pm 0.035 \text{ mHz}$, in agreement with the magnetar’s spin period at the epoch of the JWST observation. The observed pulse profile has one peak per period (although this may be due to the poor time resolution), with a lower limit on the pulsed fraction of about 10%. We compare the IR pulse profile to the NICER and NuSTAR X-ray pulse profiles and find that the IR peak overlaps with the hard X-ray peak, suggesting a magnetospheric origin for the pulsed IR emission.

1. INTRODUCTION

4U 0142+61 (4U 0142 hereafter) is one of the brightest quiescent magnetars in X-rays (Olausen & Kaspi 2014). It has a spin period of about 8.7 s, a magnetic field strength of $1.3 \times 10^{14} \text{ G}$, a characteristic age of 68 kyr, and lies at a distance of 3.6 kpc (Dib & Kaspi 2014). The X-ray luminosity, $L_X \approx 10^{35} \text{ erg s}^{-1}$, of the source in the 2-10 keV band exceeds its spin-down power $\dot{E} = 1.2 \times 10^{32} \text{ erg s}^{-1}$ by several orders of magnitude. Additionally, the source has exhibited a typical magnetar-like outburst observed by RXTE in 2007 (Gavriil et al. 2008) and by NICER in 2017 (Chu et al. 2026). In quiescence, it emits pulsed X-ray emission with an RMS pulsed fraction of about 6% at 1 keV increasing to about 20% at 60 keV (see, e.g., Figure 3 in Tendulkar et al. 2015).

4U 0142 is also one of the brightest magnetars in near-infrared (NIR) and optical (see Table 4 in Olausen & Kaspi 2014) having a K band magnitude around 20 (Hulleman et al. 2004; Durant & van Kerkwijk 2006). It is one of only three magnetars where pulsations have been detected at optical wavelengths along with SGR 0501+4516 and 1E1048.1-5937 (Dhillon et al. 2009, 2011). Optical pulsations were originally discovered in 4U 0142 in a very broad band by Kern & Martin (2002). These authors found a broad pulsed profile with a hint of two peaks per period, resembling the soft X-ray profile

but with a factor of 5–10 higher pulsed fraction. However, the optical and X-ray data were not taken simultaneously, and they did not have a phase-connected timing solution, so the phase shift between the optical and X-ray peaks was unconstrained. Dhillon et al. (2005) also detected pulsations from 4U 0142 in the i' band, with an RMS pulsed fraction of $(29 \pm 8)\%$ and a double hump structure (similar to X-rays) in the pulse profile. They used a phase-connected timing solution, valid during their optical observations, to determine that the optical peak lags the X-ray peak by 0.04 ± 0.02 cycles.

Hare et al. (2024) reported on observations of 4U 0142 with JWST using the Mid-Infrared Instrument (MIRI) low-resolution spectrometer (LRS) and the NIRCam photometer (JWST observing program #2635; Pavlov et al. 2021). The primary goal was to confirm or refute the existence of a potential fallback disk surrounding the source observed by Spitzer and reported by Wang et al. (2006). The MIRI data showed a featureless absorbed power-law spectrum, $f_\nu \propto \lambda^\alpha \propto \nu^{-\alpha}$, with a spectral index $\alpha = 0.96 \pm 0.02$, which was further supported by the NIRCam photometry in the F140M and F250M filters. These observations did not support the fallback disk scenario put forth by Wang et al. (2006), suggesting a non-thermal origin for the IR emission instead. However, a class of disk models with a temperature de-

pendence different from that suggested by Wang et al. (2006) could not be entirely excluded.

Hare et al. (2024) also found that the JWST MIRI fluxes were in good agreement with those previously measured by the Spitzer Infrared Array Camera (IRAC) at $8\ \mu\text{m}$, but there was some discrepancy that was larger than the expected calibration uncertainties between the NIRCcam photometry ($< 3\ \mu\text{m}$) and previous observations at NIR wavelengths. Previous studies have suggested that the source is variable at these wavelengths (see, e.g., Hulleman et al. 2004; Durant & van Kerkwijk 2006), which may be the cause of the discrepancy, or it may be that the IR and NIR spectral components may come from different emission regions. The picture is further complicated by the fact that the source does not seem to be variable at optical wavelengths (see, e.g., Dhillon et al. 2005; Muñoz-Darias et al. 2016) even though the absorbed power-law model fit to the JWST IR and NIR spectral energy distribution (SED) matches the optical data reasonably well when extrapolated to those wavelengths (Hare et al. 2024).

Here we report on new JWST NIRCcam observations of 4U 0142 taken in timing mode. The goal was to search for IR pulsations and compare them to those observed at X-ray wavelengths to help further discern the physical processes responsible for the emission. The phase-connected timing solution of Peng et al. (2026), based on NICER monitoring of the source that covered the time of the JWST observation, is used to compare the pulse profiles at different energies. In Section 2 we discuss the JWST observations and data reduction. In Section 3 we discuss the time-integrated photometry of 4U 0142, the phase folding of the IR and X-ray data, and the analysis of the JWST timing data. The discussion of these results is contained in Section 4. Lastly, we summarize our findings and conclusions in Section 5.

2. OBSERVATIONS AND DATA REDUCTION

2.1. JWST observations

JWST’s Near Infrared Camera (NIRCcam; Rieke et al. 2023) observed 4U 0142 on 2024 August 18. A 19.268 s acquisition exposure was taken in the F335M filter using the SUB32TATS subarray ($2'' \times 2''$ field of view) to ensure the source was placed appropriately on the detector for the time-series observation (TSO). For the TSO we used the F410M and F070W filters, with pivot wavelengths of $4.083\ \mu\text{m}$ and $0.705\ \mu\text{m}$ and bandwidths of $0.436\ \mu\text{m}$ and $0.128\ \mu\text{m}$, for the long-wavelength and short-wavelength channels, respectively. The TSO was carried out with the SUB64P subarray ($4'' \times 4''$ field of

view for F410M, and $2'' \times 2''$ for F070W filters, with pixels scales of $0.063''\text{pix}^{-1}$ and $0.031''\text{pix}^{-1}$ respectively).

The start and end times of the TSO were MJD 60540.6272905 and MJD 60540.6505413, which corresponds to a total duration (time span) $T_{\text{span}} = 2008.88$ s. Here and below the times are Barycenter Dynamical Times, TDB. We used the SHALLOW4⁸ readout pattern with 10 groups per “integration ramp”, with each group including 4 frames (plus 1 skipped frame). In total the observation included $N = 800$ integration ramps, having durations of $\Delta t_{\text{ramp}} = T_{\text{span}}/N = 2.5111$ s, with the effective exposure time of $\Delta t_{\text{exp}} = 2.45784$ s in each ramp (smaller than Δt_{ramp} due to the one skipped frame per group). This corresponds to the total exposure time $T_{\text{exp}} = N \Delta t_{\text{exp}} = 1966.272$ s.

2.2. X-ray Observations

4U 0142 has been regularly monitored with the NICER observatory (Gendreau et al. 2016) since 2019 March with a bi-weekly cadence. Recently, Peng et al. (2026) presented a phase-coherent timing solution with a validity range spanning MJD 58504 to 60730 or 2019 January 21 to 2025 February 24. We use this timing solution to phase-fold the NICER and NuSTAR data for comparison with the JWST data. We reduce and clean the NICER data utilizing the `nicer12` tool part of NICERDAS version v15. We cleaned the data by limiting the undershoot rate to be less than 100 and the overshoot rate to be less than 10 and extracted data only from observations that occurred during orbit night. We barycenter-correct the cleaned event files using the `barycorr` tool, which is included in HEASoft version 6.36, using the source position from Peng et al. (2026) and the JPL planetary ephemeris DE440. Finally, we merged all cleaned event files into one for ease of analysis.

A 41 ks observation using the NuSTAR (Harrison et al. 2013) was taken on 2022 September 20–21 (MJD ~ 59843), simultaneously with the first JWST MIRI+NIRCcam observation. Thanks to the phase-coherent timing solution from Peng et al. (2026), this dataset can still be used to compare the hard X-ray pulse profiles with those in the IR from JWST. The NuSTAR data were reduced in the same way as described in Hare et al. (2024), except that we barycentered the event arrival times using the source position from Peng et al. (2026) and the JPL planetary ephemeris DE440 before analysis was performed.

⁸ See <https://jwst-docs.stsci.edu/jwst-near-infrared-camera/nircam-instrumentation/nircam-detector-overview/nircam-detector-readout-patterns#gsc.tab=0>.

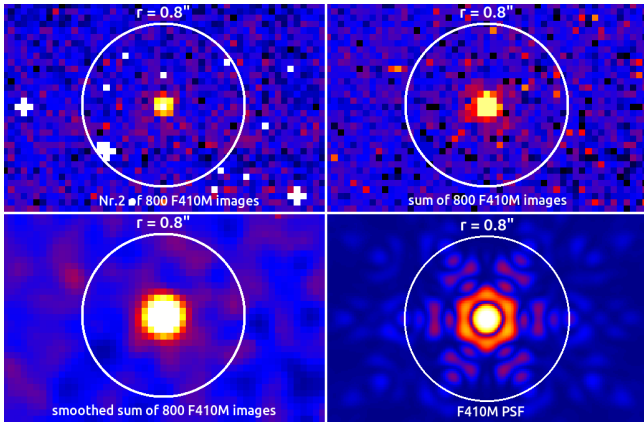


Figure 1. The NIRCcam F410M TSO data of the target region. Upper left: The second of the 800 integration ramp images. The white pixels are bad pixels. Upper right: Sum of all 800 ramp images. NaN values for bad pixels are set to 0. No smoothing was applied. Lower left: Same image as upper right, but smoothed. Lower right: WebbPSF for F410M as downloaded from the JWST webpage. No smoothing was applied. Note that the four images have different scales, limits, and adapted color scales to highlight the target/PSF region.

3. DATA ANALYSIS

3.1. Time-integrated image and photometry

For NIRCcam F410M, the image obtained in one of the 800 integration ramps and the sum of the 800 integration ramp images are shown in Figure 1. The white pixels in the upper left panel of Figure 1 are flagged as ‘bad’ in all integrations. The target’s brightness distribution (lower left panel) was visually compared with the expected point spread function in the F410M filter (lower right panel) to check for indications of telescope jitter. No indication of such jitter was seen. We use the image derived from the average of the 800 integration ramps and a corresponding bad pixel mask for our photometry. To measure the (average) flux density of 4U 0142, we employ different source aperture sizes centered on the target. To subtract the background and evaluate its contribution to the photometric error, we use the approach of “empty background apertures” (e.g., Guillot et al. 2019; Abramkin et al. 2022; Hare et al. 2024). Using an aperture of $0''.156$ (2.5 pixels) radius with encircled energy fraction (EEF) of 0.65 (see the JWST documentation on NIRCcam Point Spread Functions⁹), we obtain a $f_{F410M} = 22.9 \pm 0.6 \mu\text{Jy}$ (see Table 1 in Appendix A for details).

⁹ <https://jwst-docs.stsci.edu/jwst-near-infrared-camera/nircam-performance/nircam-point-spread-functions/#NIRCcamPointSpreadFunctions-Encircledenergy&gsc.tab=0>

For the F070W, the summed 800 integrations did not yield a target detection. We use the source position as well as 26 background positions to estimate upper bounds for the source flux (Guillot et al. 2019; Kashyap et al. 2010), using multiple aperture sizes, see Table 1. We obtain 3σ upper bounds of 0.9–1.2 μJy , depending on aperture radius. In addition to the NIRCcam TSO exposures, we used the 19 s acquisition exposure of 2024 August 18 to measure the flux density at 3.4 μm . Unfortunately, there is a bad pixel located $\approx 0''.06$ from the source leading to an unreliable flux measurement, so we excluded it from Figure 2. Details of the F335M photometry can be found in Appendix A (also see Table 1).

3.2. Re-analysis of the previous spectral fit with updated calibration

Hare et al. (2024) noticed changes of the best-fit model parameters for the MIRI LRS spectrum of 4U 0142 caused by changes in the instrument’s calibration. Furthermore, the calibration of NIRCcam and MIRI have continued to mature as more data is taken and the instruments are better understood. Therefore, to check if the updated calibration has had any major impacts on the best-fit model, we re-extracted the NIRCcam photometry and MIRI LRS spectrum from the observations reported in Hare et al. (2024). We followed the procedures outlined in that work, using the updated calibration version 1.20.2 for MIRI LRS and NIRCcam (Bushouse et al. 2025). We used the pipeline extracted LRS spectrum for MIRI and followed a similar approach for the NIRCcam photometry as outlined in the previous section for F410M filter. We obtained $f_{F140M} = 5.2 \pm 0.3 \mu\text{Jy}$ and $f_{F250M} = 14.6 \pm 0.3 \mu\text{Jy}$, consistent with the previously published values within 1σ . We did not include the NIRCcam F410M photometry in this analysis since it was taken at a different epoch and the source may exhibit variability. Note that the MIRI LRS and previous NIRCcam photometry were taken very close in time.

We jointly fit the MIRI LRS spectrum and NIRCcam photometry from the F140M and F250M filters with an absorbed power-law, $f_\nu = f_0(\lambda/\lambda_0)^\alpha 10^{-0.4A_\lambda}$. We find best-fit values of $A_V = 3.9 \pm 0.1$, $f_0 = 60.1 \pm 0.3 \mu\text{Jy}$ at $\lambda_0 = 8 \mu\text{m}$, and $\alpha = 0.95 \pm 0.01$ with a reduced chi-squared $\chi_\nu^2 = 4.0$ (see Figure 2). These values are in good agreement with $A_V = 3.9 \pm 0.2$, $f_0 = 59.4 \pm 0.5 \mu\text{Jy}$, and $\alpha = 0.96 \pm 0.02$, found by Hare et al. (2024), suggesting that the updated calibration does not have a large impact on the best-fit model parameters. The new reduced chi-squared is about a factor of 2 lower than found by Hare et al. (2024), and is mainly due to larger, more realistic error bars on the MIRI LRS

spectral data points. However, it still suggests that the errors are somewhat underestimated. Therefore, we increase the uncertainties by a factor of two, which gives $\chi^2_\nu = 0.99$, to calculate the errors in the best-fit parameters reported above in this paragraph. The data, best-fit model, and F410M photometry are shown in Figure 2. It is clear that the F410M filter photometry is significantly below the interpolation of the best-fit power-law model by about $5 \mu\text{Jy}$, or $\sim 20\%$ (see Section 4 for further discussion).

3.3. Timing analysis of the NIRCam data

We extracted the light curves from a 3×3 pixels ($0''.189 \times 0''.189$) source region centered on 4U 0142. Nine 3×3 pixels squares offset from the source were chosen for the background evaluation (see Figure 3). The net source light curve was obtained by subtracting the mean of the background light curves from the light curve of the source region. Each of the light curves is given by flux density values in the 3×3 pixels regions in $N = 800$ equal time intervals $\Delta t_{\text{ramp}} = 2.5111\text{s}$, with the total time span $T_{\text{span}} = N \Delta t_{\text{ramp}} = 2008.88\text{s}$. The source dominates the background, $0.4 \pm 0.2 \mu\text{Jy}$ per 3×3 pixels region, with a mean time-averaged background-subtracted source flux of $\bar{f}_\nu \pm \delta \bar{f}_\nu = 12.7 \pm 0.2 \mu\text{Jy}$, which is about 55% of the total (aperture-corrected) flux of the magnetar at $4.1 \mu\text{m}$. We checked that this aperture maximizes the signal in the timing analysis reported in Section 3.3.1.

3.3.1. Power spectrum of the NIRCam data

We calculated the Lomb-Scargle (LS) periodogram to search for the spin period of the magnetar using the astropy implementation of the LS algorithm (VanderPlas 2018; Astropy Collaboration et al. 2022). The barycenter-corrected times from the mid-point of each light curve time bin, provided in the calibrated JWST files, were used to construct the power spectrum. The length of the observation sets the minimum frequency of ≈ 0.5 mHz, while the $t_{\text{samp}} = t_{\text{ramp}} = 2.5111\text{s}$ sampling time gives a Nyquist frequency $\nu_{\text{Nyq}} = (2t_{\text{samp}})^{-1} = 199.116$ mHz, so we searched for pulsations in this frequency range. We used a step size of $\delta\nu = (100T_{\text{span}})^{-1} \sim 0.004978$ mHz, which includes an oversampling factor of 100, corresponding to a total of roughly 40,000 frequencies searched. We calculated the power spectrum, shown in separate panels of Figure 4, using the source light curve without subtracting the background, the mean (across the 9 regions) background light curve, and the background-subtracted source light curve.

The power spectrum of the background-subtracted light curve shows two high peaks at frequencies

$\nu_1 = 115.059 \pm 0.035$ mHz and $\nu_2 = 168.079 \pm 0.035$ mHz, with unnormalized LS powers of 54.1 and 39.7, respectively (see Figure 4). The highest peak lies close to the anticipated frequency of the magnetar pulsations (associated with the NS spin), $\nu_{\text{spin}} = 115.07724616(4)$ mHz at the mid-point of the JWST observation (i.e., MJD 60540.6389159), calculated from the timing model of Peng et al. (2026) using the Code for Rotational-analysis of Isolated Magnetars and Pulsars (CRIMP¹⁰). The offset between these frequencies is 0.018 ± 0.035 mHz, i.e., ν_1 coincides with ν_{spin} within statistical uncertainties.

Although one might speculate that the second highest peak is caused by another periodic process in the magnetar (e.g., a small object orbiting the neutron star on a $\sim 10^9$ cm radius orbit), a more natural explanation is that it is an alias connected with data sampling and the presence of second harmonic in the signal. For a sampling frequency $\nu_{\text{samp}} = (t_{\text{samp}})^{-1} = 2\nu_{\text{Nyq}}$ and a pulsed signal from the magnetar that contains several harmonics at frequencies $k\nu_{\text{spin}}$ ($k = 1, 2, \dots$), one can expect aliases at frequencies $\nu_{a,k} = \nu_{\text{samp}} - k\nu_{\text{spin}}$ (see, e.g., Eq. (46) in VanderPlas 2018). The frequency of the $k = 1$ alias, $\nu_{a,1} = 283.155$ mHz, lies above the Nyquist frequency, but $\nu_{a,2} = 168.077$ mHz coincides with the frequency ν_2 with a negligibly small offset of 0.002 ± 0.035 mHz. Thus, the presence of this alias peak in the power spectrum implies the presence of a second harmonic in the IR pulsations.

We carried out some additional checks to further substantiate this hypothesis. We first checked that the peak at this frequency (as well as the peak at the spin frequency $\nu_1 \simeq 115$ mHz) is seen in the source region in 400 ramps (≈ 1000 s) sub-samples of the entire data set. This proves that both the 115 mHz and 168 mHz peaks are persistent throughout the entire observation. To check that the 168 mHz pulsations are connected with the magnetar (i.e., an alias of the spin period), we treated one of the 9 background squares as the source region and subtracted the background determined from the remaining 8 background squares. The background-subtracted LS periodogram did not show a detectable signal at 168 mHz, further supporting that the signal is an alias of the magnetar’s spin frequency. Finally, we checked that the alias $\nu_{a,1}$ is indeed seen in the power spectrum at 283.163 mHz, which also has a negligibly small offset of 0.008 mHz.

¹⁰ <https://github.com/georgeyounes/CRIMP>

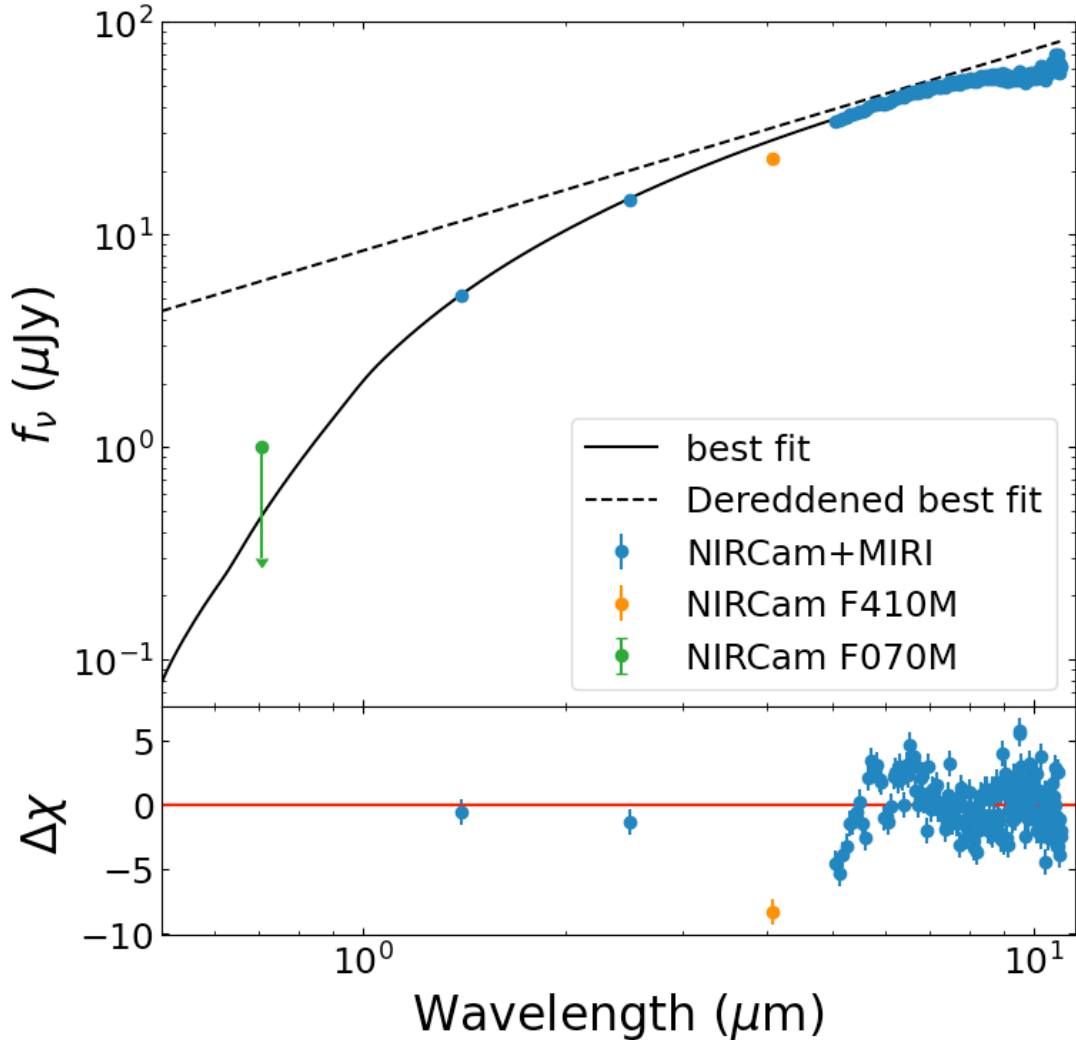


Figure 2. Best-fit absorbed power-law model to the MIRI LRS and NIRCам F140M and F250M photometry and corresponding residuals, $\Delta\chi = (\text{data} - \text{model})/\text{error}$, obtained with more recent and improved detector calibrations. Note that the F070W and F410M fluxes were not used in this fit as the data were obtained at different epochs. The fit is in good agreement with that from Hare et al. 2024. The dereddened best-fit model is shown by the dashed line. The error bars in the bottom panel correspond to $\pm 1\sigma$.

3.3.2. *Folded light curves and pulsed fractions of the IR pulsations*

Figure 5 shows phase-folded light curves at the frequency ν_1 measured by the NIRCам observations. In the phase-folded pulse profile we see one peak per period, with a width $\delta\phi \approx 0.3$ ($\delta t \approx 2.6$ s). Using this pulse profile, we calculate a “peak-to-trough” pulsed fraction¹¹ $p_{\text{amp}} = 8\% \pm 1\%$ (or an “RMS pulsed fraction” $p_{\text{RMS}} = 6\% \pm 1\%$).

It is important to note, however, that the finite time resolution suppresses the amplitude and power in a k -

th harmonic of a signal by factors $\xi_k = \text{sinc}(\pi k \nu t_{\text{ramp}})$ and ξ_k^2 , respectively (see Appendix B), which distorts the pulse profile and reduces the pulsed fraction. At $t_{\text{ramp}} = 2.51$ s, as in the NIRCам timing observation, the suppression factors for the first two harmonics are $\xi_1 = 0.87$ and $\xi_2 = 0.54$. Since the suppression of the pulsed fraction depends on the unknown relative strengths and phases of the signal harmonics, we cannot quantitatively correct it for the finite time resolution, but we can expect the true pulsed fraction to exceed the above values (e.g., $p_{\text{amp}} > 10\%$).

3.4. *Comparison of the IR and X-ray Pulse profiles*

To compare the discovered IR pulsations with the X-ray pulsations, we need an X-ray timing solution ap-

¹¹ See, e.g., Hare et al. (2021) for different definitions of pulsed fractions and their relation to each other.

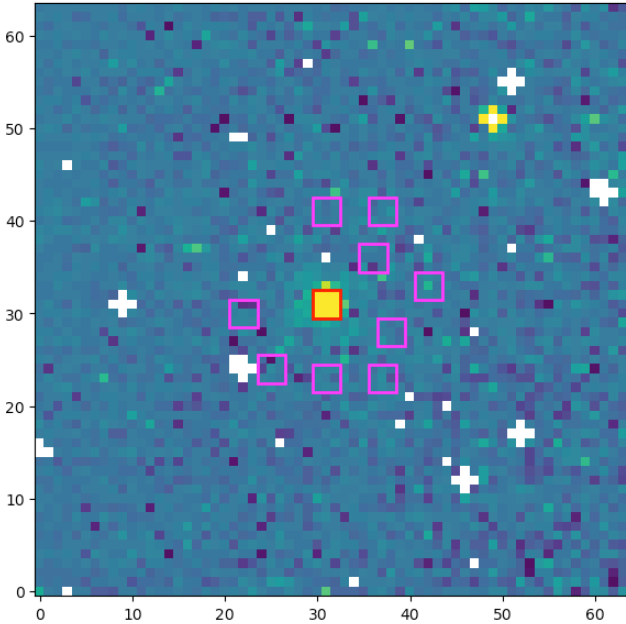


Figure 3. F410M filter image from a single integration ramp of the timing observation of 4U 0142. The white pixels correspond to known bad pixels which are masked in the calibrated images. Red shows the source region, and magenta shows the nine background regions used for the analysis.

plicable at the epoch MJD 60540 of the NIRCcam timing observation. A phase-connected timing solution has been provided by Peng et al. (2026), who analyzed X-ray pulsations detected over 6 years of NICER monitoring of 4U 0142 between MJD 58504.0–60730.1. This timing solution has RMS residuals of ~ 61 ms, or 0.7% of the magnetar’s spin period, with the maximum TOA residuals being offset by about 0.03 in phase. This solution shows two spin-down glitches, at the epochs MJD 59540 and 59850, with frequency jumps of $\Delta\nu_{g1} = -1.25(9) \times 10^{-8}$ Hz and $\Delta\nu_{g2} = -5.42(9) \times 10^{-8}$ Hz, respectively. Coincidentally, the second glitch occurred about 7 days after our previous JWST and NuSTAR observations. In Tables 5 and 6, Peng et al. (2026) provide both the 6-year solution with glitches included (Table 5 of that paper) and separate solutions in three time segments: before the first glitch (S1), between the glitches (S2), and after the second glitch (S3). These authors noticed slight (but statistically significant) differences of NICER pulse shapes in different segments (see their Figure 5), but no pulse variations were noticed within the segments. Therefore, we use the global timing solution¹² to phase

¹² Note that there is a sign error in the $\Delta\phi_{g1}$ and $\Delta\phi_{g2}$ in Table 5 of Peng et al. (2026), confirmed by private communication with Peng et al. (2026), which we correct for when phase folding our data.

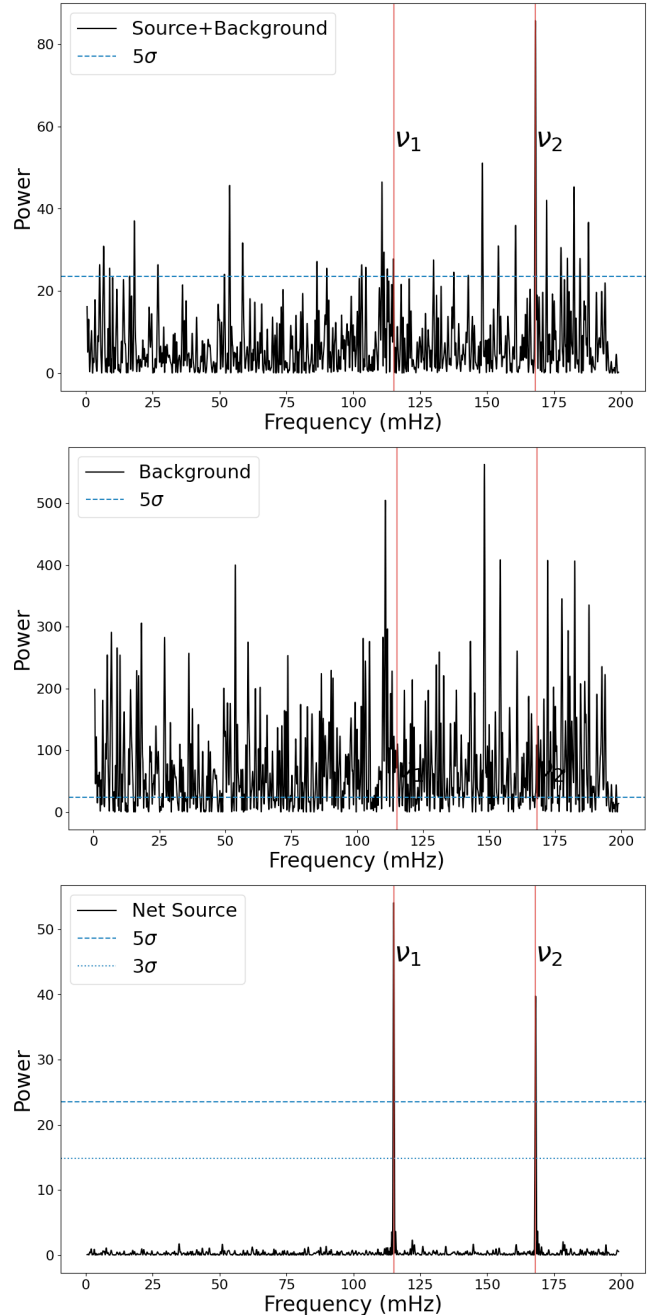


Figure 4. Lomb-Scargle periodograms of the source region without background subtraction (top), mean of the background regions (middle), and source region with background subtracted (bottom). The red solid lines show the magnetar spin peak at $\nu_1 \simeq 115$ mHz and the aliased peak $\nu_2 \simeq 168$ mHz. The blue horizontal dotted and dashed lines in the bottom panel shows the power corresponding to a 3σ and 5σ trials-corrected significance, respectively. Only the 5σ trials-corrected significance is shown in the top and middle panels.

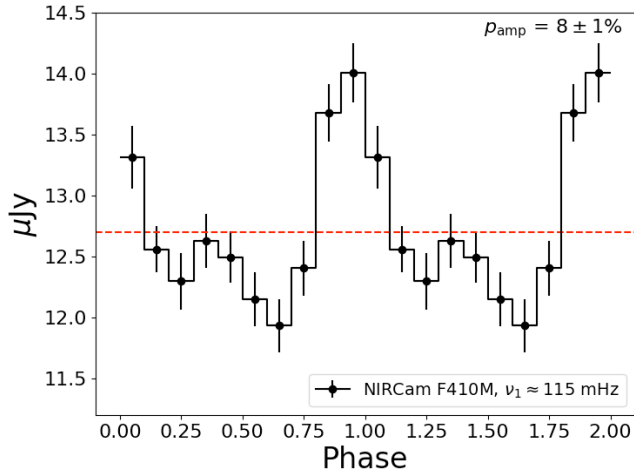


Figure 5. Binned phase-folded NIRCcam light curve for $\nu = \nu_1$ (i.e., the spin period of the magnetar). The reference time corresponding to phase 0 is MJD 60540.63881582. The red dashed line shows the time-averaged flux of the source.

fold the NICER data using the PINT python package (Luo et al. 2021; Susobhanan et al. 2024).

Given that there were differences in the pulse shapes between segments, we split the data into two epochs. Epoch 1 spans the MJD range after the first glitch from MJD 59540 to 59850, while Epoch 2 spans the MJD range after the second glitch from MJD 59850 to 60726. Note that the NuSTAR and JWST time series observations occurred in Epoch 1 and Epoch 2, respectively. The reference time corresponding to phase 0 of the Peng et al. (2026) timing solution, closest to the midpoint of the JWST TSO, is MJD 60540.63881582 and was calculated using CRIMP.

In the comparison between the IR and X-ray pulsations, we need to take into account the phase precision of the corresponding pulse profiles. The absolute timing accuracy of JWST has been shown to be on the order of 0.1 s (Shaw et al. 2025), corresponding to ~ 0.01 of the magnetar’s spin period. However, the poor time resolution of JWST has a much larger impact on determining the precise phase where the IR pulse profile peaks. The precision with which the NIRCcam pulsation phase can be measured is estimated as $\sigma_\phi \sim w_\phi (S/N)^{-1} \approx 0.064$, where $w_\phi = \nu_1 \Delta t_{\text{ramp}} \approx 0.3$ is the phase resolution ($\Delta t_{\text{ramp}} \simeq 2.5$ s is the time resolution), $S/N = p(\bar{f}_\nu / \delta \bar{f}_\nu) \approx 4.7$ is the signal-to-noise ratio for the pulsed flux (\bar{f}_ν and $\delta \bar{f}_\nu$ are the time-averaged flux density and its uncertainty in the 3×3 pixel region chosen for the analysis; see Section 3.3), and p is the pulsed fraction. This gives a rough estimate of 0.064 for the determination of the phase of the IR pulse peak. However, given that the pulse shape is not sinusoidal, and the poor

time resolution can wash out the pulse structure (e.g., the double-peaked pulse profile), the true uncertainty may be larger.

Figure 6 shows the folded NICER and IR pulse profiles from Epoch 2 (left panels) and the NICER and NuSTAR pulse profiles from Epoch 1 (right panels). The X-ray pulse profile shows two strong peaks in the 0.5–10 keV energy band around phases 0.1 and 0.66. The first peak, dominated by the hard power-law tail of the magnetar’s spectrum, persists throughout the entire X-ray energy range of 0.5–78 keV, changing shape with energy. The second peak is most prominent in the 0.5–3 keV energy range and virtually disappears in the 8–20 keV band. It is associated with thermal emission from a heated region of the neutron star surface, with a contribution from a soft power-law spectrum (see, e.g., Tendulkar et al. 2015). Previous studies have found that the RMS pulsed fraction of the X-ray emission grows with energy, from $\sim 5\%$ at 1 keV to $\sim 20\%$ above 20 keV (Tendulkar et al. 2015), consistent with the strong pulsations of the hard peak at high energies shown here. The IR peak, along with a rough estimate of the uncertainty of the peak phase due to the poor time resolution, is shown as a gray band in all the panels of Figure 6.

4. DISCUSSION

The timing analysis of the NIRCcam F410M data enabled the detection of pulsations with the magnetar’s spin frequency, $\nu_{\text{spin}} \simeq 115$ mHz, known with a much higher precision from X-ray observations (see Section 3.4). In the phase-folded light curve (Figure 5) we see one broad peak per period, with a width $\delta\phi \approx 0.3$ and a pulsed fraction $p_{\text{amp}} = 8\% \pm 1\%$. We should note, however, that the shape of these pulsations is distorted by the poor time resolution of our NIRCcam observation, $\Delta t_{\text{ramp}} \simeq 2.51$ s $\simeq 0.29 P_{\text{spin}}$, so that we cannot exclude the possibility that more than one peak would be seen if observed with better time resolution. Moreover, the poor time resolution suppresses the pulsations, which means that the intrinsic pulsed fraction may be substantially larger than the measured value.

Some hints as to the nature of the discovered IR pulsations may be provided by comparing them to the well-studied X-ray pulsations of 4U 0142 (see, e.g., Tendulkar et al. 2015, and references therein). The IR peak comes slightly before the hard X-ray peak (see Figure 6), with phase offsets of about -0.063 , -0.125 , and -0.075 from the NICER peak in the 0.5–10 keV band and NuSTAR peaks in the 8–20 and 20–78 keV, bands, respectively. These peak phases are consistent within the $(1-2)\sigma$ uncertainties of the IR peak phase. To more reliably measure the relative phases of the X-ray and IR pulsations

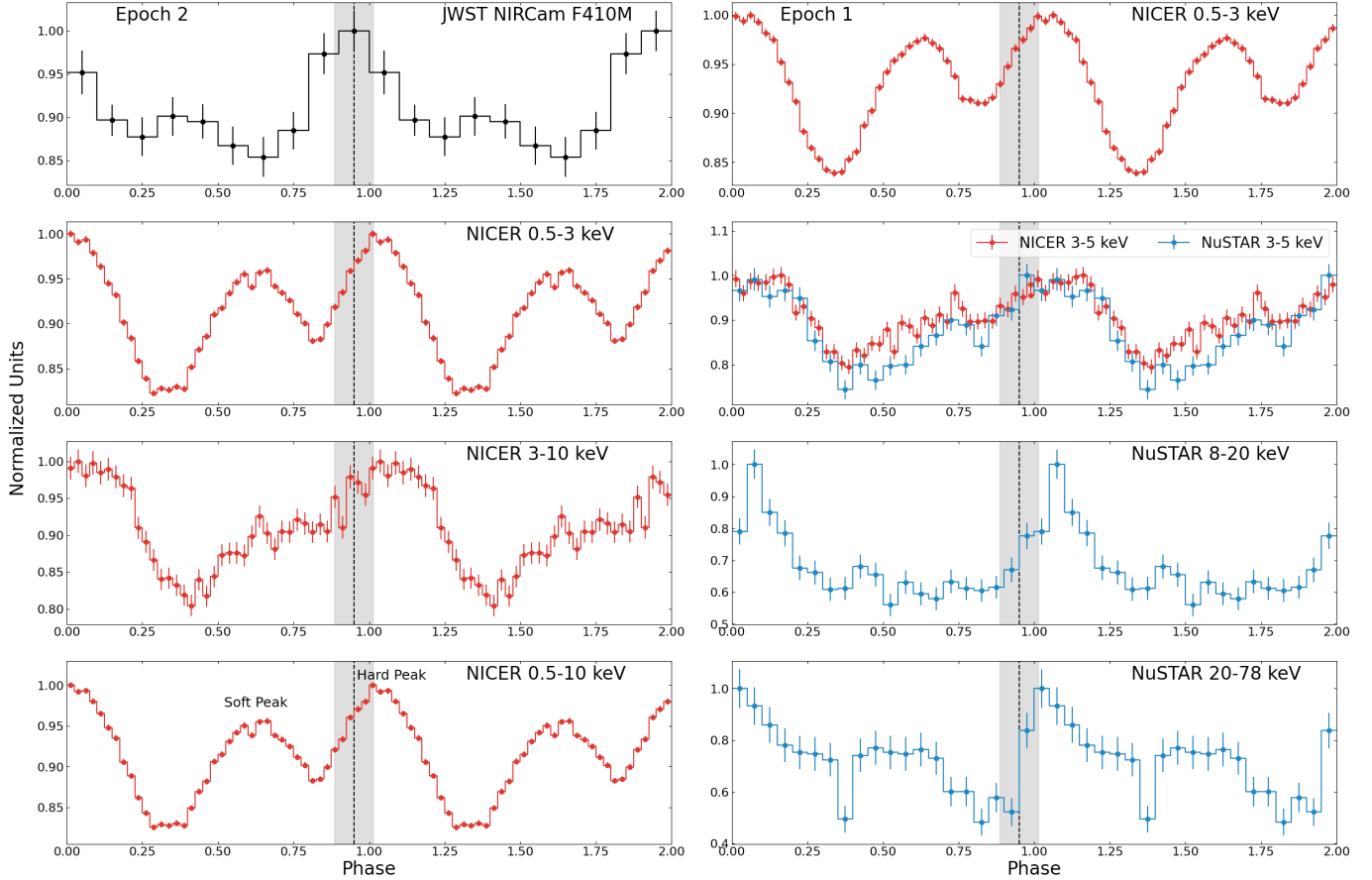


Figure 6. Binned phase-folded light curves for JWST NIRCcam, NICER, and NuSTAR observations using the timing solution presented in Table 5 of Peng et al. (2026). The four left panels show the NIRCcam pulsations, detected in a ≈ 2 ks observation taken on MJD 60540.64, together with NICER pulsations in 3 energy bands from Epoch 2, spanning MJD 59850 to 60726. The four right panels show NuSTAR pulsations in 3 energy bands, observed on MJD 59843, together with NICER pulsations in 2 energy bands observed in Epoch 1, spanning MJD 59540 to 59850. The dashed black line shows the phase corresponding to the maximum of the IR pulse profile with the gray band being an estimate of the uncertainty. The reference time corresponding to phase 0 is MJD 60540.63881582.

and suggest a detailed model, IR observations with a significantly better time resolution are required. However, if the IR peak does arrive before the hard X-ray peak, it suggests that the IR and hard X-ray emission, even if connected with each other, are produced at different emission sites.

According to popular magnetar models, the nonthermal X-ray component of magnetar’s persistent emission is produced by relativistic electrons and positrons moving from the NS surface along a loop of twisted magnetic field lines and losing their energies to the resonant Compton upscattering of thermal soft X-ray photons (see, e.g., Figure 8 in Kaspi & Beloborodov 2017). The height of this loop is likely $\lesssim 10R_{\text{NS}}$. The mechanism and site(s) of the magnetar’s IR-optical emission are currently unclear. In principle, the IR-optical emission could be interpreted as coherent curvature radiation from the inner magnetosphere, at distances $\sim 10R_{\text{NS}}$

from the neutron star surface (Zane et al. 2011). However, other possibilities are not excluded. For instance, one can imagine that some originally relativistic electrons and positrons move along open magnetic field lines, decelerate down to MeV energies and produce IR-optical photons via synchro-cyclotron radiation at much larger distances from the NS. Future near simultaneous IR-optical observations (to minimize the effects of variability) and more detailed modeling of the IR-optical emission from magnetars are needed to better understand the IR-optical emission and its possible relation to the X-ray emission.

As mentioned above, the IR pulsed fraction, corrected for the time resolution, should be higher than the measured $p_{\text{amp}} = 8\% \pm 1\%$. The true pulsed fraction may be similar to $29\% \pm 8\%$, reported by Dhillon et al. (2005) from observations of 4U 0142 in the i' ($0.8 \mu\text{m}$) band, exceeding the X-ray $p_{\text{rms}} \lesssim 20\%$. This can be considered

as an additional argument against the hypothesis that the IR emission is caused by reprocessing of the magnetar’s X-ray emission by some circumstellar material (such as a fallback disk).

Another result of this work is the possible variability of the IR flux. As shown in Figure 2 and Sections 3.1 and 3.2, the flux density value measured with F410M on 2024 August 18 lies $\sim 20\%$ below the best-fit spectrum measured with MIRI LRS and NIRCcam F140M and F250M filters on 2022 September 21. 4U 0142 has shown X-ray bursts around the time of glitches, causing the flux to increase and then decay (see, e.g., Archibald et al. 2017). Several outbursts over the past decade have been reported by Chu et al. (2026), the most recent occurring on 2023 September 26, or about 1 year before the NIRCcam TSO. It is possible that the IR flux varies with the X-ray flux during these outbursts and the subsequent decay, leading to the observed variability.

There have been several models put forth attempting to explain the IR-optical emission from magnetars with disks of gaseous or dusty matter rotating around these objects, such as fallback disks formed in the aftermath of the supernova explosion. Different disk models may be able to account for some of the observed IR-optical properties, such as the pulsations (see e.g., Ertan & Cheng 2004) and long-term variability. For instance, Ertan et al. (2007) discussed an active irradiated disk for 4U 0142, which could, in principle, account for variability (e.g., due to changes in the mass-flow rate, inner disk radius, irradiation by X-ray outbursts, or disk instabilities). However, so far a comprehensive disk model that can account for all of the observed IR/optical properties, including a broad power-law spectrum, long-term variability, and pulsations that are nearly aligned with the hard X-ray pulsations is still lacking. Moreover, it seems very plausible that the observed IR-optical properties of 4U 0142 are consistent with a nonthermal (magnetospheric) origin and can be explained without invoking a disk.

5. SUMMARY

The new JWST NIRCcam observation of the magnetar 4U 0142+61 allowed us to discover pulsations of its radiation at wavelengths around $4.1 \mu\text{m}$ at the magnetar’s spin frequency $\nu_{\text{spin}} \simeq 115 \text{ mHz}$. The IR pulse overlaps with the hard X-ray pulse. This provides further sup-

port to the conclusion, based on spectral analysis (Hare et al. 2024), that the magnetar’s IR-optical emission is of a nonthermal origin, instead of thermal emission from a fallback disk as suggested by Wang et al. (2006).

The magnetar’s flux density in the F410M filter, $f_{\nu} = 22.9 \pm 0.6 \mu\text{Jy}$, is 20% lower than expected from the spectrum measured by Hare et al. (2024) two years earlier, which suggests that the IR emission is variable.

The reported exploratory timing observation was too short and done with a too crude timing resolution to fully characterize the discovered IR pulsations and explain the origin of the IR-optical magnetar emission. Given that pulsations were detected and a lower limit on the pulse fraction was measured, a more optimal observational setup can be used in the future to better characterize the IR pulsations in this source.

Software: Astropy (Astropy Collaboration et al. 2013, 2018, 2022), PINT (Luo et al. 2021; Susobhanan et al. 2024), CRIMP <https://github.com/georgeyounes/CRIMP>, ChatGPT 5.5 Pro Extended <https://openai.com/index/introducing-gpt-5-5/>

Acknowledgments: J.H. thanks Zorawar Wadiasingh for useful discussions regarding this work and Han-Long Peng for useful discussions related to their timing model. This work is based on observations made with the NASA/ESA/CSA JWST. The data were obtained from the Mikulski Archive for Space Telescopes at the Space Telescope Science Institute, which is operated by the Association of Universities for Research in Astronomy, Inc., under NASA contract NAS 5-03127 for JWST. These observations are associated with program #2635 and can be accessed via <https://doi.org/10.17909/catg-0936>. Support for program #2635 was provided by NASA through a grant from the Space Telescope Science Institute, which is operated by the Association of Universities for Research in Astronomy, Inc., under NASA contract NAS 5-03127. J.H. acknowledges support from NASA under award number 80GSFC24M0006. This work made use of Astropy:¹³ a community-developed core Python package and an ecosystem of tools and resources for astronomy (Astropy Collaboration et al. 2013, 2018, 2022). STScI is operated by the Association of Universities for Research in Astronomy, Inc., under NASA contract NAS5-26555. Support to MAST for these data is provided by the NASA Office of Space Science via grant NAG5-7584 and by other grants and contracts.

APPENDIX

¹³ <http://www.astropy.org>

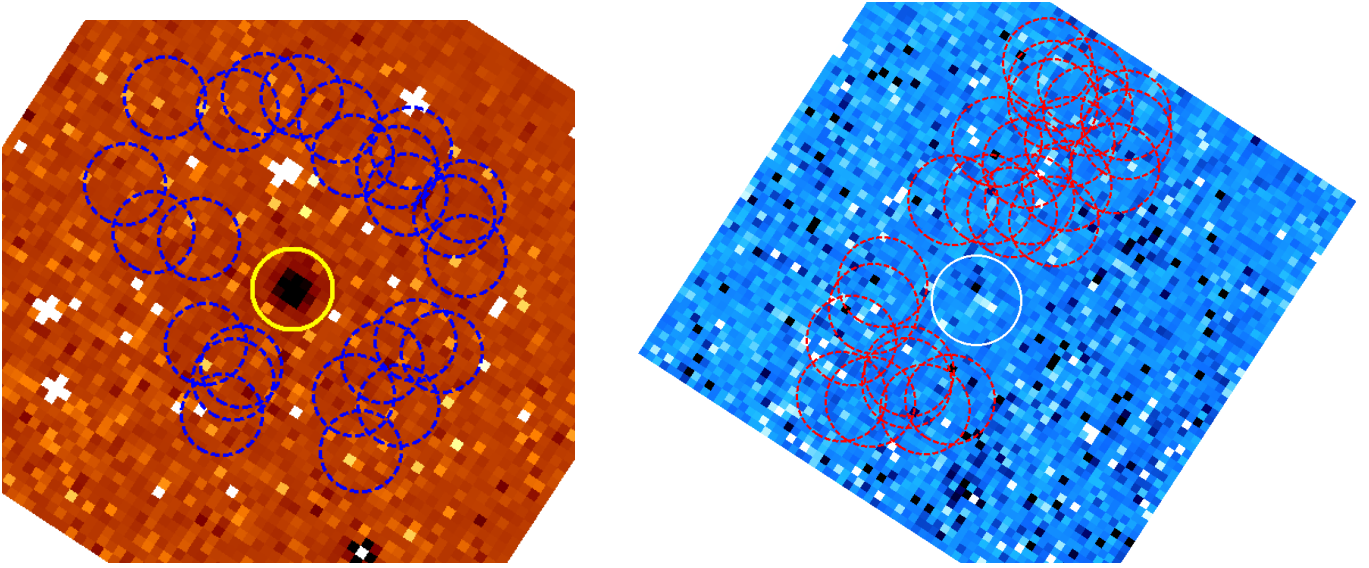


Figure 7. Locations of photometry measurement apertures for F410M (left panel) and F070W (right panel). The shown example (maximum size) apertures have radii of $0''.25$ and $0''.17$, respectively. North is up, East to the left.

A. TIME-AVERAGED PHOTOMETRY

In Table 1, we list the details of the photometry obtained from the images averaged over the 800 ramp integrations in the TSO with filters F410M and F070W and show the locations of the source and background apertures in Figure 7. For the 3σ upper bound of F070W, we list measurement results for several aperture radii up to $0''.17$, beyond which a bad pixel gets into the aperture. The upper bound, however, is relatively stable, around $1 \mu\text{Jy}$, within this aperture size range.

We also checked the photometry of the acquisition image which was done in a different filter, F335M, on the 32×32 pixels TA subarray, located at a different part of the B5 chip. The image has a bad pixel at $\sim 0''.06$ from the target center position. Although we excluded this bad pixel, we caution that the derived flux density $f_{\text{F335M}} = 11.3 \pm 0.4 \mu\text{Jy}$ may be underestimated and more uncertain due to the systematics introduced by this bad pixel.

Filter	λ_p μm	BW μm	g	t_{exp} s	r_{extr} arcsec	ϕ %	C_{tot} cnts/s	$\overline{C}_b \pm \sigma_{C_b}$ cnts/s	$\overline{C}_s \pm \sigma_{C_s}$ cnts/s	\mathcal{P}_ν $\mu\text{Jys}/\text{cnts}$	$\langle f_\nu \rangle$ or UB μJy
F410M	4.083	0.436	1.82	1806	0.156	65	196.4	11.0 ± 4.5	185.4 ± 4.5	0.0809	22.9 ± 0.6
F335M	3.362	0.348	1.82	19.15	0.05	35	80.2	30.5 ± 1.3	49.7 ± 1.7	0.0791	11.3 ± 0.4
F070W	0.705	0.128	2.05	1806	0.09	72	16.4	13.3 ± 1.6	3.1 ± 1.6	0.1034	< 1.1
					0.10	74	18.5	16.7 ± 1.7	1.8 ± 1.7		< 1.0
					0.12	75	23.9	23.8 ± 2.1	0.2 ± 2.1		< 0.9
					0.14	77	31.9	31.9 ± 2.3	0.0 ± 2.3		< 0.9
					0.15	78	36.9	36.7 ± 2.5	0.2 ± 2.5		< 1.0
					0.17	80	46.4	47.4 ± 3.5	-1.0 ± 3.5		< 1.2

Table 1. Photometry measurements of the new NIRCcam data. Here λ_p and BW are the pivot wavelength and the bandwidth of the filter, g is the gain, t_{exp} is the exposure time, ϕ is the fraction of source counts in the aperture with radius r_{extr} , C_{tot} is the total count rate in the source aperture, \overline{C}_b and σ_{C_b} are the mean and standard deviation of background count rate measurements, $\overline{C}_s = C_{\text{tot}} - \overline{C}_b$ and $\sigma_{C_s} = [(\sigma_{C_b}^2 + \overline{C}_s^2 t_{\text{exp}}^{-1} g^{-1})^{1/2}]$ are the net source count rate and its standard deviation, \mathcal{P}_ν is the count rate-to-flux conversion factor, $\langle f_\nu \rangle = (\overline{C}_s \pm \sigma_{C_s}) \mathcal{P}_\nu / \phi$ is the mean flux density, and UB = $(\overline{C}_s + 3\sigma_{C_s}) \mathcal{P}_\nu / \phi$ is the 3σ upper bound on the source flux.

B. EFFECTS OF FINITE TIME RESOLUTION

In a NIRC*am* TSO of a periodic source, one obtains a series of source flux values accumulated in equal adjacent time intervals (integration ramps) Δt_{ramp} , which can be considered as the time resolution. Unless Δt_{ramp} is much shorter than the source period, the finite time resolution distorts the detected pulsations. For instance, for purely sinusoidal pulsations with frequency ν , the signal accumulated in the n -th integration ramp ($n = 1, 2, \dots, N$) is proportional to

$$\frac{1}{\Delta t_{\text{ramp}}} \int_{t_0 + (n-1)\Delta t_{\text{ramp}}}^{t_0 + n\Delta t_{\text{ramp}}} \sin 2\pi\nu t \, dt = \sin 2\pi\nu [t_0 + (n-1/2)\Delta t_{\text{ramp}}] \text{sinc}(\pi\nu\Delta t_{\text{ramp}}), \quad (\text{B1})$$

where t_0 is the start time of the first ramp, and $\text{sinc } x = (\sin x)/x$. This equation shows that the integrated signal in each ramp is proportional to the original value of the sinusoidal signal in the middle of the ramp multiplied by the suppression factor $\xi = \text{sinc}(\pi\nu\Delta t_{\text{ramp}})$, which does not depend on ramp number. This means that the finite time resolution does not change the signal frequency, but it reduces the signal amplitude and pulsed fraction by the reduction factor ξ , and reduces the Fourier power of the signal by the factor ξ^2 . At $\nu\Delta t_{\text{ramp}} < 1$ these factors monotonically decrease with increasing $\nu\Delta t_{\text{ramp}}$, becoming zero at $\nu\Delta t_{\text{ramp}} = 1$.

If the signal contains harmonics $k > 1$, then the amplitude of the k -th harmonic is suppressed by the factor $\xi_k = \text{sinc}(\pi k\nu\Delta t_{\text{ramp}})$, while the power of the k -th harmonic is suppressed by the factor ξ_k^2 . This implies that the finite time resolution not only leads to suppression of the signal amplitude and power, but also distorts its shape.

REFERENCES

- Abramkin, V., Pavlov, G. G., Shibarov, Y., et al. 2022, *ApJ*, 924, 128. doi:10.3847/1538-4357/ac3a6f
- Archibald, R. F., Kaspi, V. M., Scholz, P., et al. 2017, *ApJ*, 834, 2, 163. doi:10.3847/1538-4357/834/2/163
- Astropy Collaboration, Price-Whelan, A. M., Lim, P. L., et al. 2022, *ApJ*, 935, 2, 167. doi:10.3847/1538-4357/ac7c74
- Astropy Collaboration, Price-Whelan, A. M., Sipőcz, B. M., et al. 2018, *AJ*, 156, 3, 123. doi:10.3847/1538-3881/aabc4f
- Astropy Collaboration, Robitaille, T. P., Tollerud, E. J., et al. 2013, *A&A*, 558, A33. doi:10.1051/0004-6361/201322068
- Bushouse, H., Eisenhamer, J., Dencheva, N., et al. 2025, *Zenodo*, 1.20.2. doi:10.5281/zenodo.17515973
- Chu, C.-Y., Hu, C.-P., Enoto, T., et al. 2026, *ApJS*, 284, 1, 25. doi:10.3847/1538-4365/ae5655
- Dhillon, V. S., Marsh, T. R., Hulleman, F., et al. 2005, *MNRAS*, 363, 609. doi:10.1111/j.1365-2966.2005.09465.x
- Dhillon, V. S., Marsh, T. R., Littlefair, S. P., et al. 2009, *MNRAS*, 394, 1, L112. doi:10.1111/j.1745-3933.2009.00623.x
- Dhillon, V. S., Marsh, T. R., Littlefair, S. P., et al. 2011, *MNRAS*, The first observation of optical pulsations from a soft gamma repeater: SGR 0501+4516, 416, 1, L16. doi:10.1111/j.1745-3933.2011.01088.x
- Dib, R. & Kaspi, V. M. 2014, *ApJ*, 784, 37. doi:10.1088/0004-637X/784/1/37
- Durant, M. & van Kerkwijk, M. H. 2006, *ApJ*, 652, 576. doi:10.1086/507605
- Ertan, Ü., & Cheng, K. S. 2004, *ApJ*, 605, 840. doi:10.1086/382502
- Ertan, Ü., Erkut, M. H., Ekşi, K. Y., et al. 2007, *ApJ*, 657, 1, 441. doi:10.1086/510303
- Gavriil, F. P., Dib, R., & Kaspi, V. M. 2008, 40 Years of Pulsars: Millisecond Pulsars, Magnetars and More, 983, 234. doi:10.1063/1.2900150
- Gendreau, K. C., Arzoumanian, Z., Adkins, P. W., et al. 2016, *Proc. SPIE*, The Neutron star Interior Composition Explorer (NICER): design and development, 9905, 99051H. doi:10.1117/12.2231304
- Guillot, S., Pavlov, G. G., Reyes, C., et al. 2019, *ApJ*, 874, 2, 175. doi:10.3847/1538-4357/ab0f38
- Hare, J., Volkov, I., Pavlov, G. G., et al. 2021, *ApJ*, 923, 2, 249. doi:10.3847/1538-4357/ac30e2
- Hare, J., Pavlov, G. G., Posselt, B., et al. 2024, *ApJ*, 972, 176. doi:10.3847/1538-4357/ad5ce5
- Harrison, F. A., Craig, W. W., Christensen, F. E., et al. 2013, *ApJ*, 770, 103. doi:10.1088/0004-637X/770/2/103
- Hulleman, F., van Kerkwijk, M. H., & Kulkarni, S. R. 2004, *A&A*, 416, 1037. doi:10.1051/0004-6361:20031756
- Kashyap, V. L., van Dyk, D. A., Connors, A., et al. 2010, *ApJ*, 719, 1, 900. doi:10.1088/0004-637X/719/1/900
- Kaspi, V. M. & Beloborodov, A. M. 2017, *ARA&A*, 55, 1, 261. doi:10.1146/annurev-astro-081915-023329
- Kern, B. & Martin, C. 2002, *Nature*, 417, 527. doi:10.1038/417527a
- Luo, J., Ransom, S., Demorest, P., et al. 2021, *ApJ*, 911, 1, 45. doi:10.3847/1538-4357/abe62f
- Muñoz-Darias, T., de Ugarte Postigo, A., & Casares, J. 2016, *MNRAS*, 458, L114. doi:10.1093/mnras/rlw024

- Olausen, S. A. & Kaspi, V. M. 2014, *ApJS*, 212, 6.
doi:10.1088/0067-0049/212/1/6
- Pavlov, G. G., Kargaltsev, O., Hare, J., & Posselt, B. 2021, JWST Proposal. Cycle 1, ID. #2635
- Peng, H.-L., Weng, S.-S., Ge, M.-Y., et al. 2026, *ApJ*, 999, 1, 85. doi:10.3847/1538-4357/ae4007
- Rieke, M. J., Kelly, D. M., Misselt, K., et al. 2023, *PASP*, 135, 028001. doi:10.1088/1538-3873/acac53
- Shaw, A. W., Kaplan, D. L., Gandhi, P., et al. 2025, *AJ*, 169, 1, 21. doi:10.3847/1538-3881/ad8eb1
- Susobhanan, A., Kaplan, D. L., Archibald, A. M., et al. 2024, *ApJ*, 971, 2, 150. doi:10.3847/1538-4357/ad59f7
- Tendulkar, S. P., Hascöet, R., Yang, C., et al. 2015, *ApJ*, 808, 32. doi:10.1088/0004-637X/808/1/32
- VanderPlas, J. T. 2018, *ApJS*, 236, 1, 16.
doi:10.3847/1538-4365/aab766
- Wang, Z., Chakrabarty, D., & Kaplan, D. L. 2006, *Nature*, 440, 772. doi:10.1038/nature04669
- Zane, S., Nobili, L., & Turolla, R. 2011, *High-Energy Emission from Pulsars and their Systems*, 21, 329.
doi:10.1007/978-3-642-17251-9_26